Tribology International 186 (2023) 108619

Contents lists available at ScienceDirect

Tribology International

journal homepage: www.elsevier.com/locate/triboint

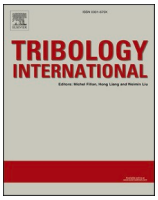

Nanostructured Al_2O_3/graphene additive in bio-based lubricant: A novel approach to improve engine performance

Sunil Jayantha Hettiarachchi [a,*], James Bowen [b], Matthew Kershaw [b], Ioan-Alexandru Baragau [a,c], Adela Nicolaev [c], Suela Kellici [a]

[a] London Centre for Energy Engineering, School of Engineering, London South Bank University, London SE1 0AA, UK
[b] Faculty of Science, Technology, Engineering, and Mathematics, Open University, Milton Keynes MK7 6AA, UK
[c] National Institute of Materials Physics, Atomistilor 405A, 077125 Magurelc, Ilfov, Romania

ARTICLE INFO

Keywords:
Friction
Wear
Lubrication
Additives
Nanofluid
Graphene

ABSTRACT

Personal and industrial use of internal combustion engines (ICEs) is projected to continue until 2050 and beyond. Yet demands to reduce global dependence on petrochemicals and fossil fuel-derived lubricants are increasing and environmentally necessary. New strategies for maintaining and enhancing ICE performance by reducing friction, wear, fuel consumption, and exhaust emissions will reduce the depletion of mineral and fossil fuel reserves and environmental pollution. This paper reports the tribological enhancement of nano-bio lubricants formulated using 2D nanocomposites of Al_2O_3/graphene as novel additives in coconut oil, whose performance as a lubricant compares favorably with the mineral-based engine oil 15W40. Structural, compositional, and morphological characterization of the Al_2O_3/graphene nanocomposite revealed an ultra-fine particle size (< 10 nm) with spherical/laminar morphology and a rich sp^2 domain, exhibiting a consistent colloidal stability when formulated as nanofluid. Through the use of various characterization techniques, including friction and wear analysis we gained valuable insight into the tribological mechanism. Our optimization of this 2D tribological system using coconut oil formulation resulted significant reductions in the coefficient of friction (28 %), specific fuel consumption (8 %), and exhaust pollutant emissions (CO, SO_2, and NO_x). This work demonstrates the benefits of using nano-bio lubricant formulated using coconut oil and 2D-based hybrids as base stock and additives, delivering solutions to global challenges such as improving fuel consumption while reducing environmental pollution; solutions that can be transferred to other areas where lubricants are a necessity.

1. Introduction

In today's contemporary dynamic industry and environmentally conscious society, it is an escalating necessity to mitigate the environmental pollution caused by internal combustion engines (ICEs). The focus of this research is saving energy and reducing the usage of fossil fuel and mineral reserves via enhanced lubrication, which reduces friction and wear in ICEs.

In this context, bio-lubricants and nanomaterial additives can play a pivotal role, where scientists are researching innovative ways to produce hybrid nano/bio-lubricants. Examples of nanomaterials added to lubricants include metal oxides of Al_2O_3, TiO_2, $TiSiO_4$ and recently reported 2D graphene derivatives. For example, Gulzar et al. [1] used 0.75 wt% of $TiSiO_4$ (~ 50.0 nm) as a nano-additive in palm-trimethylolpropane (PTMP) ester and observed a 68 % reduction in the coefficient of friction (COF) and a 50 % reduction in the wear volume. Abdulrahiman et al. [2] observed the enhancement of tribological performance by adding 0.50 wt% of nano CuO (~ 50.0 nm) to coconut oil (CCO). Abere et al. [3] utilized nanoparticles of Al_2O_3 (20.0 nm), SiO_2 (5.0–15.0 nm) and graphite (35.0–80.0 nm), 0.10 wt% with untreated rapeseed oil and multigrade formulated mineral oil 15W40 and observed the enhanced tribological performance with combined additives; nanoparticles with zinc-dialkyldithiophosphate (ZDDP), which confirms the nanoparticle's ability to work in synergy with ZDDP. Talib et al. [4] tested nanoparticles of hexagonal boron nitride in many concentrations with modified jatropha oil and observed a COF (76 %) and wear (26 %) reduction with a 0.55 wt% concentration. Jibin et al. [5] acknowledge the optimized COF and wear reduction performance by the combination of CCO and hybrid Ce-Zr nanoparticles, 0.62 wt%, with improved thermo-physical properties. Luo et al. [6] studied the tribological

* Corresponding author.
E-mail address: hettiars@lsbu.ac.uk (S.J. Hettiarachchi).

https://doi.org/10.1016/j.triboint.2023.108619
Received 21 March 2023; Received in revised form 6 May 2023; Accepted 16 May 2023
Available online 16 May 2023
0301-679X/© 2023 The Author(s). Published by Elsevier Ltd. This is an open access article under the CC BY license (http://creativecommons.org/licenses/by/4.0/).

properties of spherical Al_2O_3 nano powder (78.0 nm) and revealed the reduction of COF (17.6 %) and wear scar diameter (WSD, 41.8 %) of the worn surface compared to the reference oil. Ali et al. [7] emphasized the enhanced tribological performance of Al_2O_3 nanoparticles (8.0–12.0 nm), 0.25 wt% as an additive in formulated mineral oil 5W30 and revealed reductions of COF (35 %) and wear rate (21 %). Meng et al. [8] who studied the tribological properties of graphene, used mineral oil 10W40 as base-stock to blend with Ag/graphene nanocomposite (Ag/GN: spherical, 4.0–10.0 nm) as nano-additives and observed the reduction of COF (30.4 %) and WSD (27.4 %) with 0.06–0.10 wt% concentration. Similarly, Song et al. [9] used graphene nano sheets/-MoS_2 nanocomposites as an ICE lubricant additive and reported reductions in COF and WSD. Finally, Song et al. [10] utilized α-Fe_2O_3 nanorod/graphene composites and reported tribological enhancement. This is due to the ultrafine atomic thickness, high surface area and spherical, laminar, or laminar/spherical surface morphologies of 2D materials, which can infiltrate through rubbing asperities or create a synergistic ball bearing effect between the contacting surfaces to reduce friction and wear.

Bio-lubricants have been demonstrated to exhibit superior biodegradability, low toxicity, higher viscosity index, compared to mineral-based lubricants. They are also more recyclable and renewable and are thus good candidates to substitute for mineral-based lubricants [11]. Nonetheless, one set of limitations observed for bio-lubricants are their low temperature characteristics; wax formation, poor cold flow, high pour point (PP), and low oxidative stability, all of which are qualities in need of enhancement [11]. There are numerous bio-lubricants containing plant oils or animal fats in use with reasonably similar molecular structures, commonly known as triglyceride molecules [11]. CCO has been selected in this research as the bio-base stock, because of the excellent availability. We will examine the tribological characteristics of nano/bio lubricants on components within internal combustion engines (ICE).

The ICE is a heat engine, which converts chemical energy into kinetic energy via a combustion process with an approximate thermal efficiency around 20–30 % for gasoline and diesel engines [12]. Energy losses through heat transfer, sound generation and friction contribute to the low thermal efficiency [12]. Ali et al. [7] estimated that 17–19 % of power generated by an engine will be lost through friction, of which perhaps the relative motion of the piston ring assembly and cylinder liner interface will account for 40–50 % of frictional power losses within an ICE: this was later confirmed by Jia et al. [13].

This paper investigates the tribological behavior of nano/bio lubricants on ICE components. Particular emphasis is placed on the piston ring cylinder liner interface, where the use of nanoparticles as engine oil additives with bio-based sample formulations will be compared with the performance of a conventional multigrade mineral-based lubricant (15W40). The objective is to identify the optimal engine oil formulation which reduces friction and wear, thus improving fuel economy and reducing exhaust emissions. It therefore follows that optimizing the ICE performance saves energy and reduces the depletion of fossil fuels and mineral reserves for a stable and sustainable environment.

2. Experimental methodology

2.1. Materials

Mineral-based multigrade engine oil 15W40 was selected as the reference oil, which is widely used in both gasoline and diesel engines. Al_2O_3 and graphene (G) were selected to synthesise an Al_2O_3/G nanocomposite as an additive to blend with CCO as bio-based stock for sample formulation. Nano Al_2O_3/G was synthesized via a thermal annealing route [14].

CCO was procured from local mills in Sri Lanka. Reference oil "15W40″ (CEYPETCO® /CALTEX®) had the following specification, with parameter values in the range specified: Total base number (TBN): 9.8–10.2 (mg KOH g^{-1}); Kinematic viscosity at 40 °C: 109–115 (mm^2 s^{-1}); Kinematic viscosity at 100 °C: 14.1–15.1 (mm^2 s^{-1}); Viscosity Index: 130–137 (unitless). 15W40 was purchased from the Ceylon Petroleum Cooperation (CEYPETCO), Sri Lanka and sunflower oil (SF), styrenated phenol (SP), and oleic acid (OA) were from Glorchem Enterprise, Sri Lanka. Nanomaterials: Al_2O_3 and graphene were procured from XF-NANO Co., Ltd., China. All other chemicals: pour point depressants (PPDs), antioxidants (AOs), and viscosity modifiers (VMs), including KOH and polymer polymethylmethacrylate (PMMA - M_w 15,000 g mol_j^1 were procured from Sigma-Aldrich, UK and Fisher Scientific, UK.

2.2. Synthesis and characterization of nanomaterials

Nanocomposite Al_2O_3/G was synthesized using Al_2O_3 nanoparticles and graphene via traditional thermal annealing [14]. Initially 95.0 wt% Al_2O_3 and 5.0 wt% of graphene were mixed manually in a beaker with 300 mL of isopropanol. Then the mixture was sonicated for 1 h using an ultrasonic mixer (Kerry - KS 200) followed by centrifuging at 8000 rpm (utilizing Thermo/Sorvall RC 6 plus centrifuge). Thereafter, the slurry was kept in an oven and heat treated for 3 h at 280 °C (using Micrometric Flow-Prep 060). Nitrogen gas was used to prevent oxidation during processing. The final product was characterized using transmission electron microscopy (TEM) [JEOL-JEM-2100], X-ray powder diffraction (XRD) [Bruker D8 Advance with DIFFRAC.EVA software], Raman [Horiba LabRam HR Evolution], and X-ray photoelectron spectroscopy (XPS) [Axis Ultra DLD setup].

2.3. Blending and stability studies of sample lubricants

A total of 5 blended lubricants were used including reference oil 15W40 (S1). All the samples were made and blended after formulating CCO with enhanced physicochemical properties. Descriptions and chemical compositions of samples are summarized in Table 1. Nano-additive Al_2O_3/G was utilized in three different weight concentrations (0.10, 0.25 and 0.50 wt%) with the base stock to study the effect of nanoparticle concentration on the tribological performance and the dispersion stability of the sample lubricants. Oleic acid (OA; cis-9-octadecenoic acid; $C_{18}H_{34}O_2$) [6,15] was selected as the surfactant when blending nanoparticles, because of the high polarity resulting from the monounsaturated fatty acid structure [1,16]. The concentration of OA reduces the surface tension of the lubricating oil. This effect is due to the presence of unsaturated C═C double bonds and the polar nature of the substance. This, in turn, influences the adsorption of nano additives to the formulation molecules, preventing agglomeration. Moreover, the -COOH group attracts the substrate, while the +R group repeals it, resulting in the boundary layer formation that enhances lubrication. To improve suspension stability, ultrasonic mixing (Kerry - KS 200) was used (2 h) followed by agitation (2 h) using a magnetic stirrer [Thermo Scientific – Cimarec$^+$].

2.3.1. Stability tests of sample blends

Dispersion stability of nanoparticles was investigated using a double beam UV–vis spectrophotometer (Shimadzu – UV – 1800). The absorbance of selected samples (best performing) was examined from 0 to 72 h in 24-hour intervals and continued up to five weeks in weekly intervals.

2.4. Performance tests

Performance tests consisted of friction and wear analyses to investigate frictional force (FF), COF, morphologies, elemental deposition, and the surface texture of wear surfaces with different lubricants.

2.4.1. Friction tests

Friction tests were implemented using a linear reciprocating

Table 1
Sample description and elemental composition of sample lubricants.

Sample No	Base oil		Surfactant (OA)	Additives	
	Composition	Concentration (wt%)	Concentration (wt%)	Composition	Concentration (wt%)
S1	15W40	100	N/A	N/A	N/A
S2	FCO	100	N/A	N/A	N/A
S3	FCO	98	1.90	Al_2O_3/G	0.10
S4	FCO	98	1.75	Al_2O_3/G	0.25
S5	FCO	98	1.50	Al_2O_3/G	0.50

Key: 15W40 – reference oil; FCO – formulated coconut oil; OA – oleic acid.

tribometer (LRT) test rig (DUCOM TR – 282), to simulate the reciprocating motion of a piston ring/cylinder liner interface of an ICE. The custom-built "WINDUCOM-2010″ software executed the preprogramed test protocol, displayed COF and FF with associated waveforms in real time, acquired and processed experimental data, and controlled the test rig during the tests. All LRT tests were performed as per the ASTM G181-11 standards, using all 5 samples including reference oil S1 (Table 1). Piston ring and cylinder liner segments were used as test specimens with 2 variables (load and sliding velocity) at an elevated temperature (140 °C) to simulate real ICE operation. Test conditions were five different loads (120, 140, 160, 180, and 200 N) with five variable sliding velocities with reference to sliding frequencies (15, 20, 30, 40, 50 Hz). A total of 25 load/velocity combinations with 360 s for each combination equated to a 9000 s test duration for each sample.

Test specimens were aligned axially and laterally to avoid mismatch of curvatures during all tests since specific contact pressures generated at the interface of the piston ring cylinder liner segments during LRT tests are inversely related to the contact areas of the specimens. Contact parameter is an effective limit along with load, speed and material parameters to develop a lubricant film, thick enough to separate rubbing asperities according to Reynolds' and Hammrock & Dowsons' predictions [17,18].

Test specimens were fragmented from a new piston ring and a cylinder liner from a heavy-duty Perkins, model 4000 series diesel engine to confirm that the test specimens have the same hardness as real ICE engine components. Vickers surface hardness tests were performed following ASTM E92–2017 guidelines (Table T1 in electronic supplementary information [ESI]). Fig. F1 in ESI illustrates the tribo-testing geometry of test specimens, which confirms the elliptical contact area at the interface of reciprocating concave, convex surfaces in contact [18].

2.4.2. Wear scar analyses

After the LRT tests, wear scars of the test specimens of sample lubricants (with enhanced tribological performance) were analysed via SEM and EDX (using Microscope "Pemtron PS-230″ integrated with "Oxford Instrument x-ACF" setup) and surface roughness utilizing 3D non-contact optical profilometer (Leica DCM3D).

2.4.3. Thermal and oxidative stability

Formulated coconut oil (FCO), which stands for sample S2 was also used as the base stock for samples S3, S4, and S5. The thermal and oxidative stability of FCO was analysed along with coconut oil (CCO) using a Thermogravimetric analyser (Rheometric Scientific STA 1500) and compared.

2.4.4. Analyses of rheological behavior

Rheological behavior of sample blends having improved tribological performances, (shown during LRT tests) was examined using a rheometer (Bohlin/Gemini 2 – GEM200 – 903). The test protocol uses ramping shear rates vs temperature ranging from 60° to 120°C, with step-wise increments of 20 °C.

2.4.5. Analyses of specific fuel consumption (SFC) and exhaust emissions

Fuel consumption and exhaust emissions were examined on sample lubricants with enhanced tribological performance during LRT tests. A dynamometer test rig with 4.8 kW of rated power was utilized for the investigation (ESI Table T2). Fuel consumption was tested for five load variations ending up with 25 % overload condition to study the lubricant's behavior under adverse conditions. Each test was performed three times to minimize errors. Exhaust emissions were analysed using "Technovation – FEM7″ exhaust gas analyser in order to quantify carbon, nitrogen and sulfur oxides (CO_x, NO_x, SO_x) as a percentage.

3. Results and discussions

3.1. Characterization of nanomaterials

Transmission electron microscopy (TEM), and selected area electron diffraction (SAED, inset) images with particle size distribution histograms (inset) for Al_2O_3, Al_2O_3/G, are shown in Fig. 1. These images were used to analyse the particle size, lattice fringes and ᴅ-spacing of these nanomaterials, which are vital parameters in the tribological domain [9,19]. The observations revealed the average particle size for the following metal oxide materials: Al_2O_3: 7.0 ± 0.7 nm, Al_2O_3/G: 10.0 ± 0.3 nm.

Graphene sheets have lateral dimensions of 319 ± 50 nm (Fig. 1c) [20]. Lattice fringe spacings of 0.37 ± 0.01 nm, were observed for 2D-graphene in nanocomposites of Al_2O_3/G (Fig. 1d), consistent with reported literature values [21]. The nanoparticle sizes are ultra-fine and can infiltrate through asperities of the piston ring cylinder liner interface, in comparison to the reported ICE lubrication film thicknesses, which are in macro-scale (0.1–10 μm) [22].

The XRD patterns presented in Fig. 2a confirm the nanomaterials used in this study as Al_2O_3, graphene, and their nanocomposite Al_2O_3/G. For example, XRD pattern for Al_2O_3 has phase indices of (111), (220), (311), (222), (400), (511), and (440) at $2\theta = 20.08°$, 32.4°, 37.4°, 39.5°, 45.7°, 60.7°, and 66.9° respectively (ICDD: 00–50–0741) [8,23]. The observations confirm that the alumina is in gamma phase with strong peaks at (311), (400) and (440) indices [23]. Also, XRD patterns for graphene reveal the corresponding diffraction peaks of (002) and (004) at $2\theta = 26.1°$ and 54.4° respectively [20]. In addition, the broadened peak at $2\theta = 44.3°$ represents the index (101) (ICDD: 00-041-1487). The diffraction peaks of nanocomposite Al_2O_3/G are represented in the nanoparticle compositions associated with the syntheses of the respective nanocomposite. Moreover, broadened peaks of Al_2O_3 and Al_2O_3/G suggest low crystallinity, presumably because of smaller particle sizes, which agrees with the observed SAED patterns of metal oxide phase for Al_2O_3 and Al_2O_3/G nanomaterials (Fig. 1) [8].

Fig. 2b. shows the observed *Raman spectra* for the above nanomaterials. Spectra for graphene exhibit sharp peaks at the wavenumbers of 1334.5, 1579.7 and 2686.6 cm^{-1} representing D, G, and 2D bands respectively. The G band, which is at 1579.7 cm^{-1}, is ascribed to the first order scattering of $E_{2\,g}$ phonons vibration because of sp^2 hybridization [21,24]. The D band at 1334.5 cm^{-1} is ascribed to in-plane scattering of the $A_{1\,g}$ phonon vibration, which could be attributed to the change of

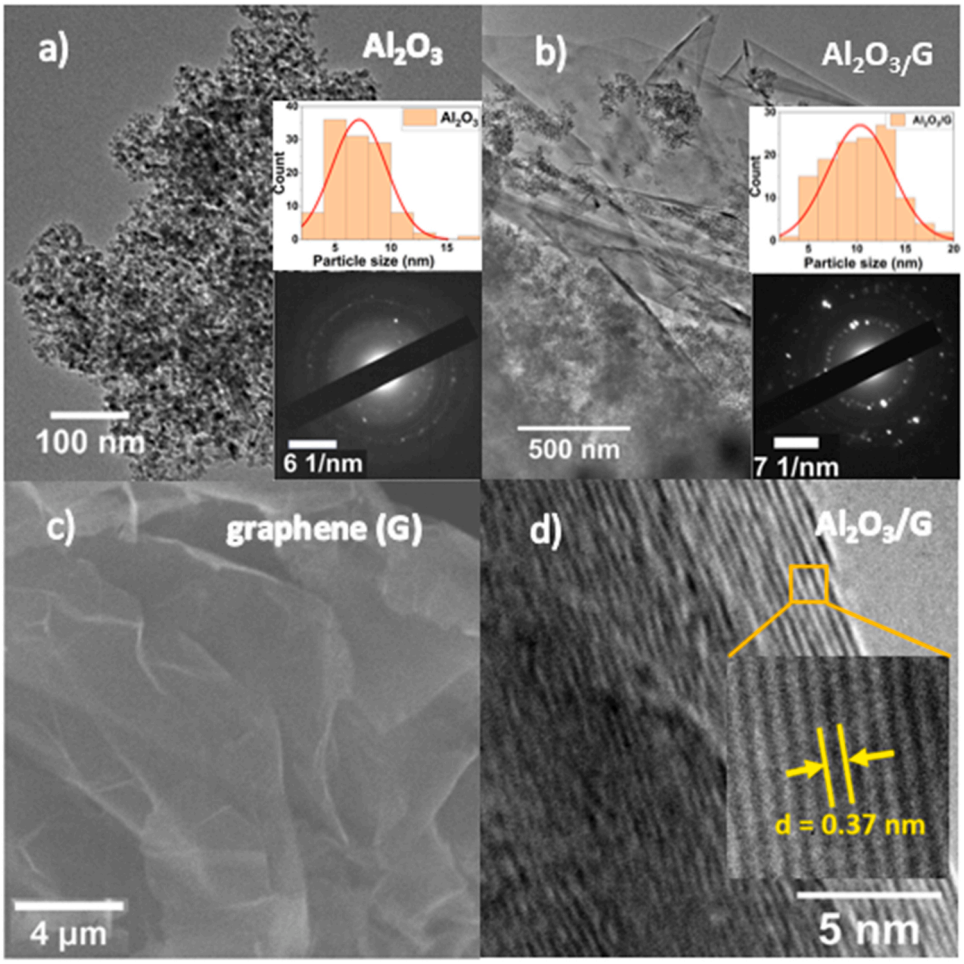

Fig. 1. Morphologies of nanoparticles; TEM with SAED patterns and particle size distribution histograms (insets) for a) Al_2O_3, b) Al_2O_3/G, c) SEM image for graphene sheets (G), d) TEM image with lattice fringe spacing (inset) for 2D-graphene sheets in nanocomposites used; Al_2O_3/G (d = 0.37 nm).

atomic bond hybridization from sp^2 to sp^3 configuration, most probably caused by the oxidation or incorporation of oxygen functional groups leading to structural defects [25]. However, the relative intensity between D and G bands i.e., I_D/I_G = 0.21 indicates a rich sp^2 domain, minimal disorder or structural defects of the graphene sheets utilized [24,25]. The 2D band at 2686.6 cm^{-1} represents double resonance enhanced A_1 phonon vibration [21].

Raman spectra for Al_2O_3 shows peaks ranging from 200 to 1200 cm^{-1}. Peaks at 240.7, 381.1, 430.6, 568.2, 713.0, 820.9, and 898.8 cm^{-1} are identical to the established data, which confirms that the material is Al_2O_3 [26]. High-intensity bands at 240–500 cm^{-1} represent Al-O vibration stretching, whereas sharp intensity bands above 500 cm^{-1} arise from the stretching of hydroxyl groups. Moderate and low-intensity bands appear in the same range indicating deformation of hydroxyl groups [26]. Raman spectra for Al_2O_3/G consists of Raman bands at 455.3, 789.9, 916.8, and 1086.1 cm^{-1} representing Al_2O_3. Graphene is represented by the bands at 1355.5, 1582.0, and 2727.9 cm^{-1}, confirming the combination of alumina and graphene within the nanocomposite. Nevertheless, Raman peaks of Al_2O_3/G are shifted towards higher wavenumbers indicating the increase in grain size (from 7.0 to 10.0 nm, Fig. 1) [27,28].

XPS analyses were performed to ascertain the elemental composition and chemical states of the nanomaterials used in the research. The observations are presented in Figs. 3 and 4, for graphene (G), and Al_2O_3 respectively. All the core level spectra of interest (C 1s, O 1s, and Al 2p) have been deconvoluted using Voigt profiles, based on the methods described by Teodorescu et al. [29]. The atomic composition has been determined by using the integral areas provided by the deconvolution procedure followed by normalization using the atomic sensitivity factors provided by Wagner et al. [30].

The survey scan for G (Fig. 3c) illustrates a higher elemental composition of C than O with C:O ratio of 18.19:1 (C: 94.3 %, O: 5.7 %), which lends further reinforcement to the Raman observations, a rich sp^2 domain with low relative intensity I_D/I_G = 0.21. In addition, expanded XPS spectra for the C 1s orbital (Fig. 3a) shows peaks at 284.6 eV, 285.0 eV, and 285.5 eV indicating three different chemical states, which could be ascribed to sp^2 C (G), C-O, (sp^3), and C═O (sp^2), respectively. In the O 1s spectra (Fig. 4b), peaks at 531.1 eV, and 532.5 eV could be assigned to C═O (sp^2) and C-O (sp^3) correspondingly, confirming less carbonyl or oxygen functional groups with the utilized graphene [27, 31].

Fig. 4(a–d) illustrates the XPS spectra for Al_2O_3 including core level details of C 1s, O 1s and Al 2p with survey scan for the same regions respectively. Peaks for C 1s at 284.6 eV, 286.1 eV, and 289.6 eV could be attributed to C-C, C-O, O-C═O indicating possible adventitious carbon. The O 1s band shows peaks representing Al-OH and Al-O-Al at 531.2 eV and 532.8 eV correspondingly. Also, the deconvoluted spectrum for Al 2p has two peaks at 74.9 eV and 75.7 eV, which could be ascribed to Al_2O_3 and $Al(OH)_3$ chemical states, respectively [32]. The results shed light on the additional diffraction peaks observed in the XRD patterns (Fig. 2a), confirming the formation of alumina-tetrahydrate ($Al_2O_3{\cdot}3H_2O$) within the Al_2O_3 nanoparticles.

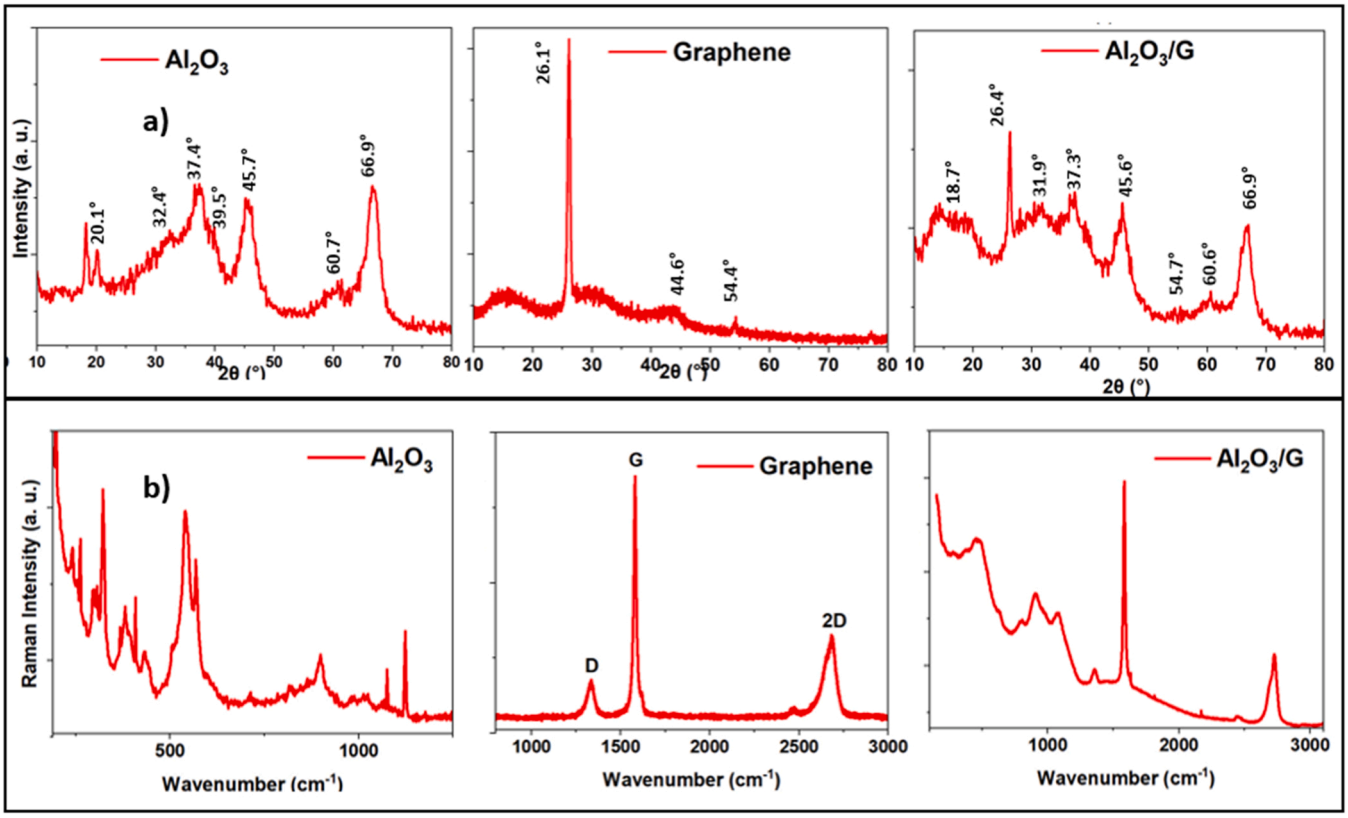

Fig. 2. Characterization results of nanomaterials used; a) XRD patterns, b) Raman spectra, for Al_2O_3, graphene, Al_2O_3/G.

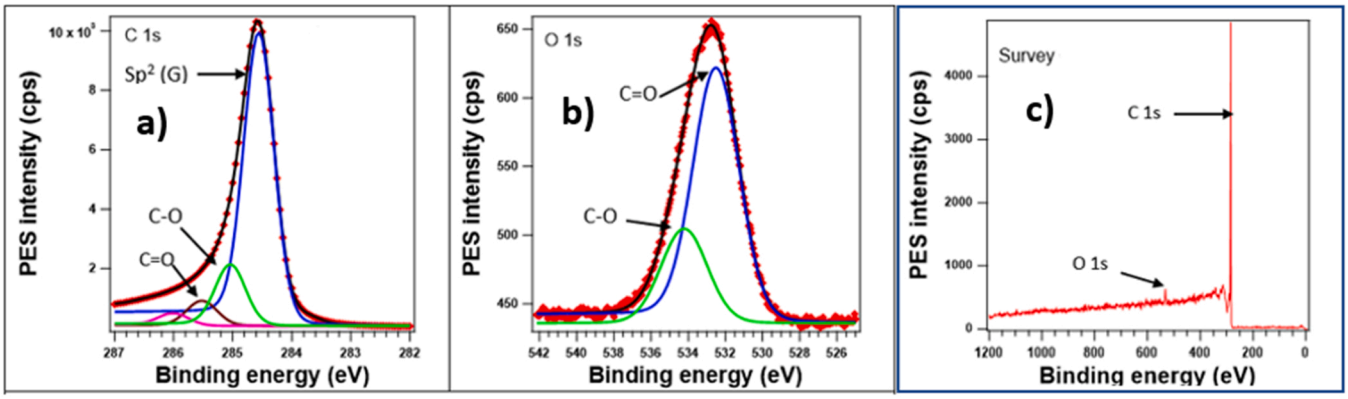

Fig. 3. XPS spectra for graphene with high resolution of a) C 1s, b) O 1s regions and c) survey scan covering C 1s and O 1s regions.

3.2. Improving physicochemical properties of CCO

Addition of SP (20 % v/v), polymer PMMA (0.50 wt%), and KOH (0.50 wt%) improved the required physicochemical properties; poor cold flow behavior, viscosity index (VI), and total base number (TBN) of CCO. Results are summarized in Table 2.

3.3. Analysis on the thermal, oxidative and shear stability of FCO

The thermal and oxidative stability of FCO was analysed with the flow of atmospheric air (79:21N_2:O_2) as the experimental background [33]. Fig. 5a-b present the thermogravimetric analysis (TGA) thermograms for CCO and FCO at 150 °C confirming improved thermal and oxidative stability of FCO under the airflow than CCO. The addition of chemicals to improve the physicochemical properties of CCO may have contributed to enhancing thermal and oxidative stability. The formation of branches in the CCO molecules is one of the suggested mechanisms to address poor cold flow. It creates additional unsaturated C═C bonds, which could explain the effect on the thermal stability of formulated CCO.

Fig. 5c-d, which present the flow behavior of samples S1 and S2 in double log scale, indicate better shear stability of FCO (S2) compared to the reference oil (S1) under increasing temperatures (60, 80, 100 and 120 °C). Flow curves for both samples indicate similar characteristics for all temperatures. The linear section of the curves indicates the power-law region suggesting non-Newtonian, pseudoplastic characteristics of liquids. Moreover, shear thickening appears to occur at high shear rates (~ log 3.8 s^{-1} and above) for both S1 and S2, yet this is a measurement artefact, attributed to dissimilar temperatures between adjacent fluid layers. If not shear thickening, most non-Newtonian fluids will reach a viscosity plateau at high shear rates according to Carreau-Yasuda and Cross model predictions [34]. On the other hand shear thickening is

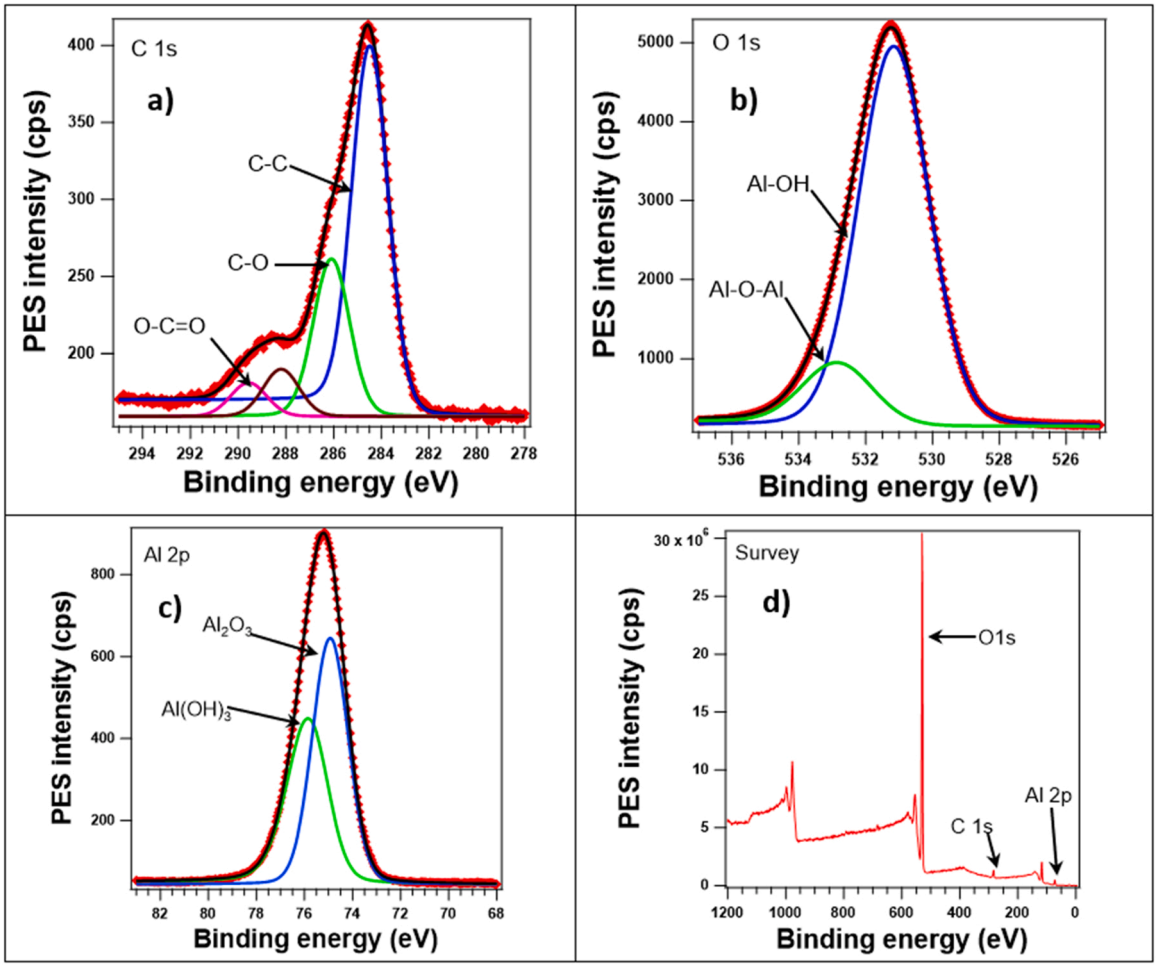

Fig. 4. XPS spectra for Al_2O_3 nanoparticles with expanded details for a) C 1s, b) O 1s, c) Al 2p orbitals with d) survey scan for C 1s, O 1s, and Al 2p regions.

Table 2
Comparison of physicochemical properties of CCO vs FCO.

Sample	TAN (mg KOH g^{-1})	TBN (mg KOH g^{-1})	Kinematic Viscosity @ 40 °C (mm^2 s^{-1})	Kinematic Viscosity @ 100 °C (mm^2 s^{-1})	Viscosity Index (VI) (dimensionless)	Pour point* (°C)
CCO	1.94–12.8	****	24.8	5.5	169	21.0
FCO	0.29	4.14	46.2	9.8	206	6.0
15W40	****	9.8	109	14.1	130	-33.0

* Measured in 3 °C intervals.

critical at high shear rates to maintain lubricant viscosity in real ICE operation.

3.4. Analysis of coefficient of friction (COF)

LRT tests were performed after formulating FCO with improved sub standards of CCO. Fig. 6 shows the COF vs time analysis for FCO (S2) and reference oil (S1) under two different test conditions, a) 120 N load with 20 Hz of sliding frequency and b) 180 N load with 50 Hz of sliding frequency, both at 140 °C elevated temperature. The results indicate that the FCO can reduce the COF by 7 % (mean) for all 25 test conditions with maximum COF reduction of 53 % under the test b), without adding any additives, compared to the reference oil (S1).

Figs. 7–9 depict the tribometer test results for samples S3, S4, and S5 with reference oil S1, under different load velocity combinations. Each data point in these figures represents an average of approximately 3500 readings, and the standard error is in the range of 2.2×10^{-6} to 2.4×10^{-5}. Therefore, error bars do not appear in these figures. Fig. 7 demonstrates the tribological behavior of formulations containing FCO with different weight concentrations of Al_2O_3/G nano-additives (S3, S4, and S5) with reference oil (S1) during LRT tests under 180 N load at 140 °C. The results show the COF vs sliding frequency graphs, which reveals that the increment of sliding frequency reduces the COF value for all samples. This is directly correlated to the angular velocity (i.e., rpm) of the mechanism regardless of the load variation, indicating an increment of EHL due to an increase in fluid pressure along with an increase in fluid entrainment velocity, which depends on the relative velocity of the surfaces in proximity [17,18]. Tribometry graphs of above samples (S1, S3, S4, and S5) for COF vs loads with 50 Hz frequency at 140 °C are shown in Fig. 8. From these graphs, it is evident that load has no effect on friction reduction when compared to the reductions observed with increasing velocity (Fig. 7), which indicates that the load parameter has the least impact when compared to the contributions of speed, material, and contact parameters [18,35].

Fig. 9 presents the results of LRT tests performed using samples S3, S4, and S5 with reference S1. Under all 25 test conditions sample S3 has

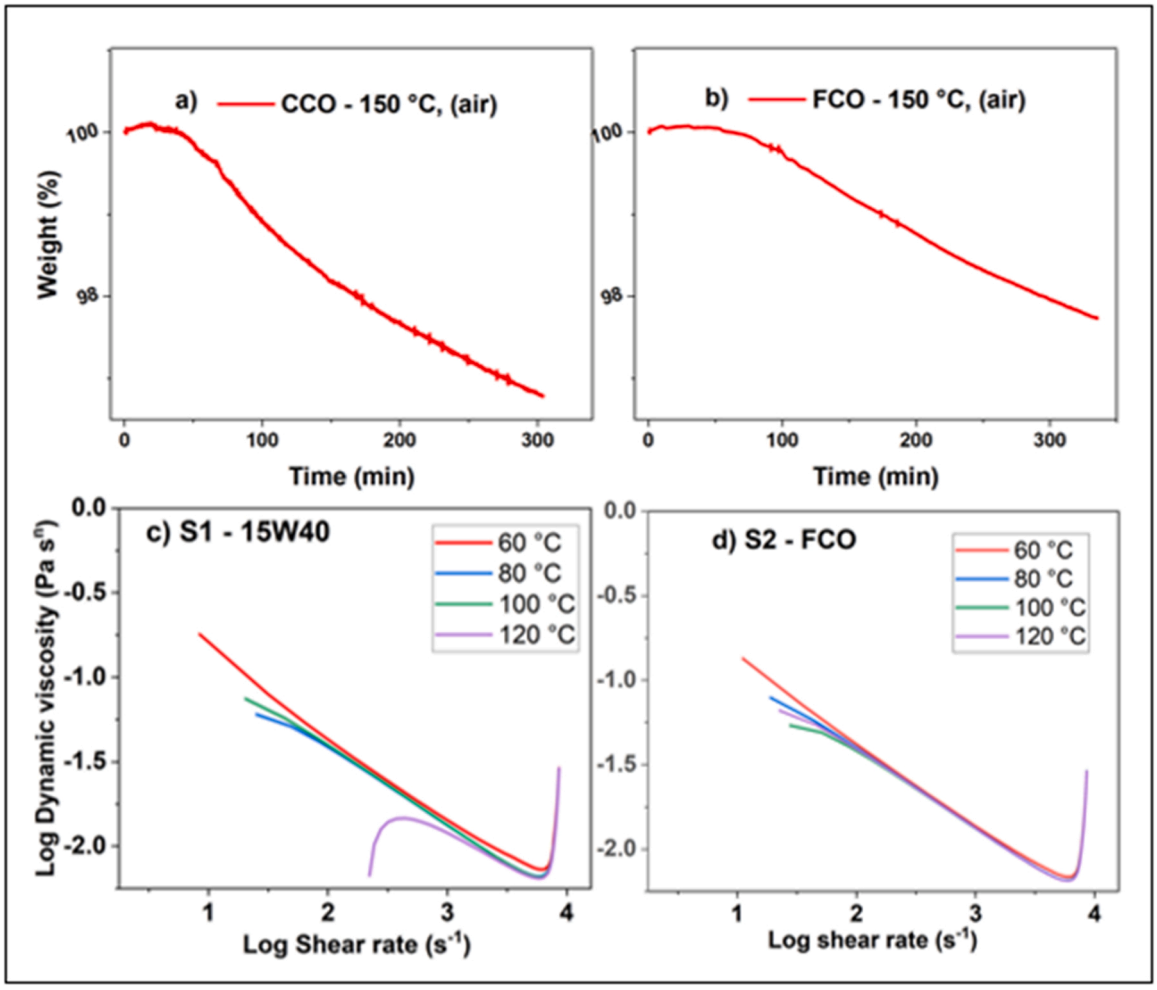

Fig. 5. TGA thermogram for weight loss analysis at 150 °C for a) CCO, b) FCO under flow of atmospheric air (21 % v/v O_2) environment and rheometric curves in log-log axes for samples c) S1, and d) S2.

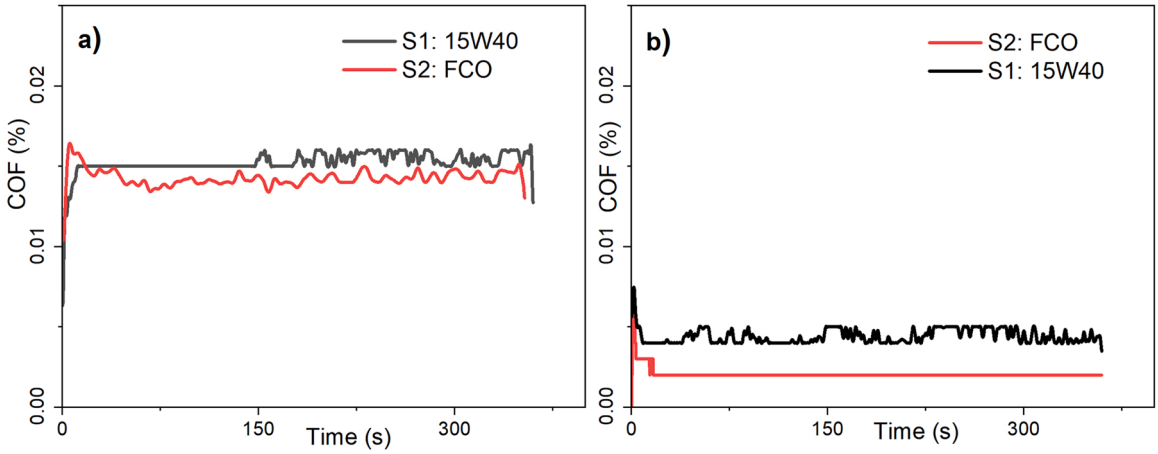

Fig. 6. Tribometry data for LRT tests; COF vs time analysis between samples S1 and S2 under two different test conditions, a) 120 N load with 20 Hz sliding frequency, b) 180 N load with 50 Hz sliding frequency, both at 140 °C.

dominated throughout with effective lubrication to reduce friction and emerged with a maximum of 59 % COF reduction for the 200 N/50 Hz load/frequency combination. The average COF reduction for all test combinations compared to S1 (reference oil) was 28 %.

A few unusual COF readings are visible from the tested samples. For example, S4 under 200 N/15 Hz, S5 under 180 N/15 Hz and S1 under 22 N/40 Hz (Fig. 9a–d), test conditions with rapid increase or decrease of COF could be ascribed to the entry of agglomerated nano-additive clusters or silicon particles to the tribo-test interface. This is one of the reasons to have 25 test conditions to minimize errors when selecting an optimum formulation.

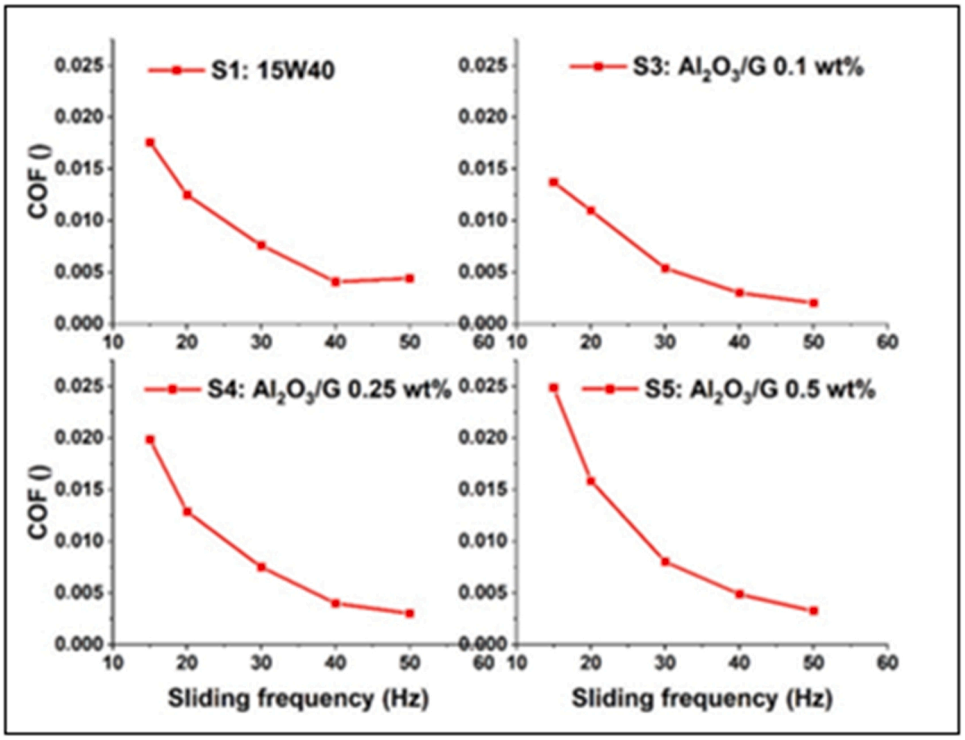

Fig. 7. Tribometry curves of LRT tests for COF vs sliding frequency analyses on sample blends containing FCO with different concentrations of Al_2O_3/G nano-additives (S3, S4, and S5) and reference oil S1 under 180 N load at 140 °C (standard error in the range of 2.2×10^{-6} to 2.4×10^{-5}).

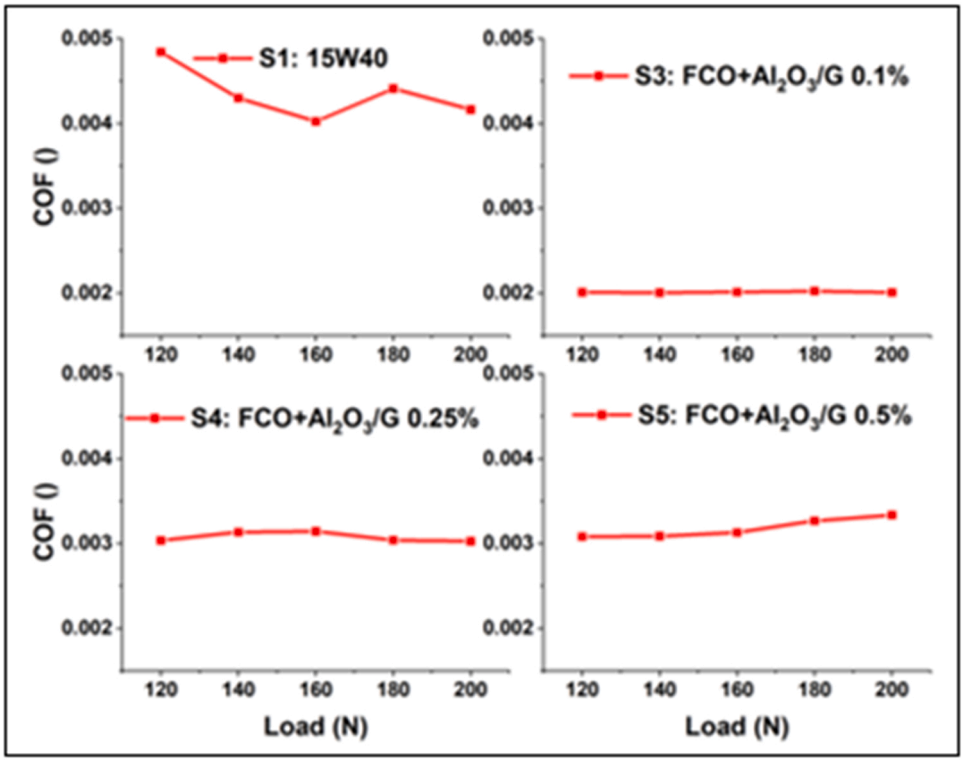

Fig. 8. Tribometry curves of LRT tests for COF vs load analyses on sample blends containing FCO with different concentrations of Al_2O_3/G nano-additive (S3, S4, and S5) with reference oil S1 under 50 Hz sliding frequency at 140 °C (standard error in the range of 2.2×10^{-6} to 2.4×10^{-5}).

3.5. Dispersion stability of formulated nano/bio-lubricants

Sample S3 was selected for absorbance tests, because of its improved tribological performance demonstrated during LRT tests among all the samples tested. The results of optical absorbance spectra show improved dispersion stability of sample S3; perhaps the low crystallinity and

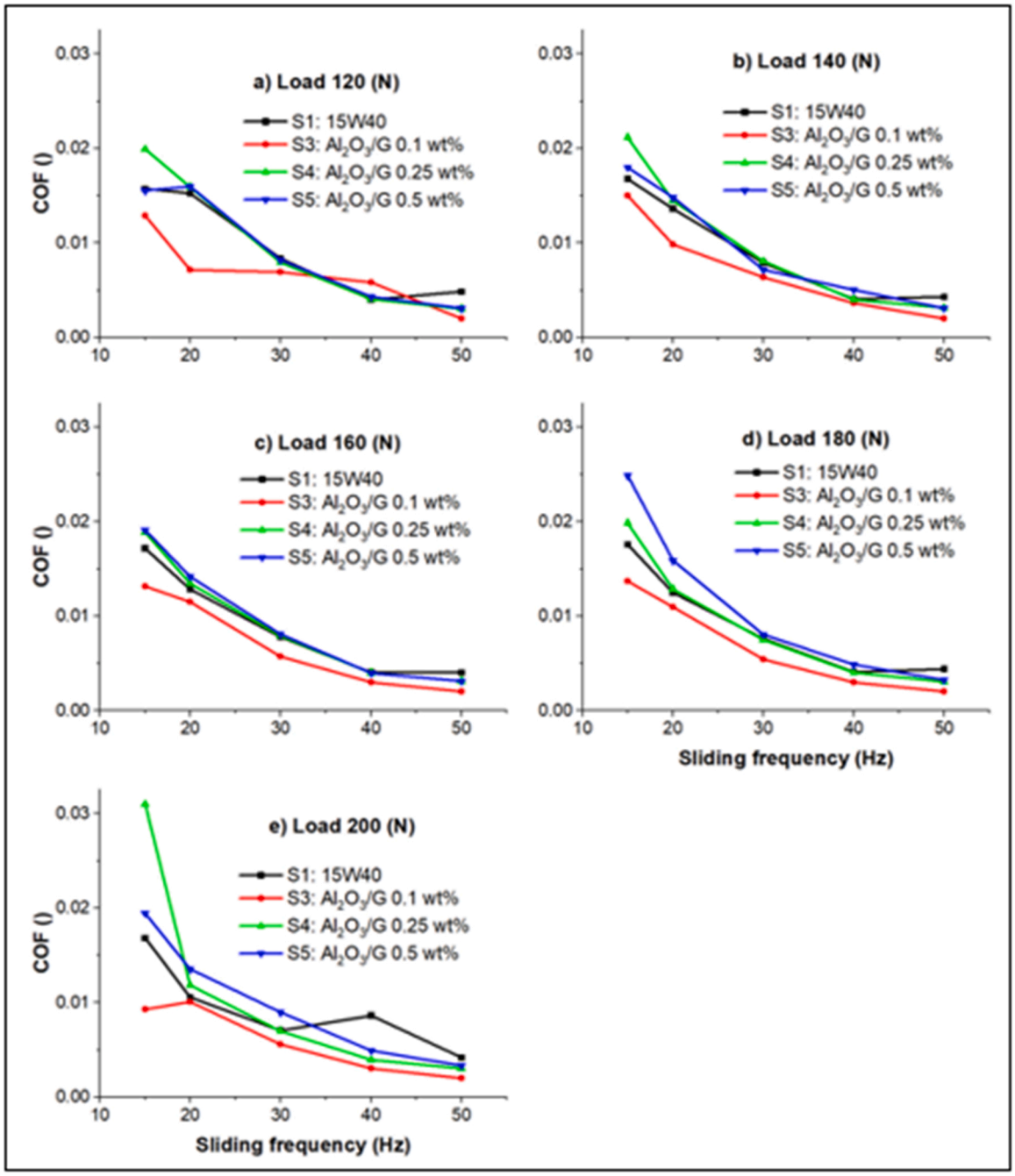

Fig. 9. LRT, tribological performance of FCO+Al_2O_3/G blends; COF vs sliding frequency curves with different loads; a) 120 N, b) 140 N, c) 160 N, d 180 N, e) 200 N, at 140° (standard error in the range of 2.2×10^{-6} to 2.4×10^{-5}).

particle size of Al_2O_3/G (Fig. 1) with the use of an ultrasonic mixer for agitation could have played a role. Moreover, S3 exhibited different degrees of sedimentation during the 0–72 h period. Fig. 10 shows the results of absorbance vs time analysis for the S3, which confirms the sedimentation of surplus nano-additive particles of S3 up to 72 h after blending, with consistent colloidal stability thereafter, throughout the experiment range [1,36].

All the samples were tested approximately one month after the blending was completed. Colloidal stability of dispersed nanoparticles is critical for any tribological application, which is achieved through thermal energy and Brownian motion of the molecules in the solution. UV–vis analysis revealed the stability of S3. During nanoparticle characterization (TEM, SAED, XRD) it is observed that Al_2O_3/G nanoparticles have laminar/ spherical morphology, and low crystallinity with a mean particle size of 10.0 ± 0.3 (nm). According to Stokes' law (which describes the settling behavior of particles in a fluid under the influence of gravity), particle size is inversely proportionate to the sedimentation rate, low crystallinity will reduce the density and hardness and laminar/spherical morphology will affect to influence the thermal conductivity of the nano additives used, which have a smaller particle size (10.0 ± 0.3 nm), properties which may have contributed to the stability of sample S3.

3.6. Wear scar analyses: SEM, EDX, and 3D none-contact optical profilometry

EDX analyses were performed along with SEM surface characterization on wear surfaces of test specimens (piston ring segments [PRS]

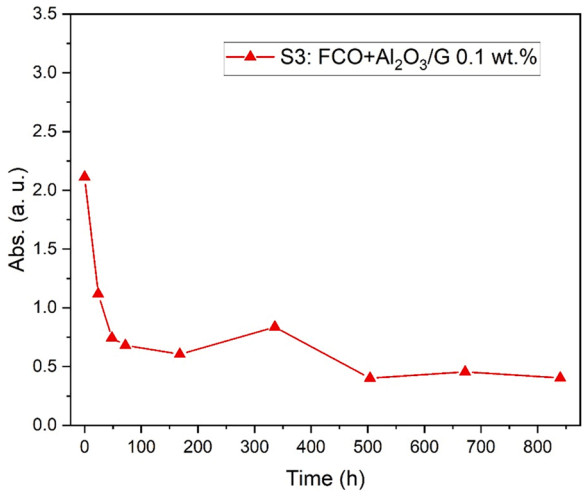

Fig. 10. Optical absorbance vs time profile for the sample S3.

and cylinder liner segments [CLS]) to evaluate elemental deposition on stroked surfaces. EDX findings for PRSs (surface area of ~ 29.45 mm^2, ESI Table T1) are presented for better accuracy. ESI Figs. F2 and F3 show the elemental spectra for unused PRS surface and for the wear surface of sample S3 after LRT tests. This is to compare elemental deposition and to assess a feasible lubrication mechanism. From the results, it is revealed that the used PRS surface of S3 has additional elemental deposition compared to the unused PRS surface (Fe, C, Si and P elements). Some additional elements are present: Ni, Cr, and Mo could come from the outer coating of the PRS, O from the atmospheric air because of the combustion process and elements K and Al on the surface could arise from the usage of KOH during the formulation of FCO. The sample S3 contains Al_2O_3/G as nano-additives, which agrees with the observation of Ali et al. (2016) [8]. Deposition of Al nanoparticles and other elements on the PRS surface of S3 (Fig. F3) suggests a protective layer formation assisted by secondary mending and polishing effect by Al_2O_3/G nanomaterials. Furthermore, Fig. F2 reveals 65 % of Fe deposition on the surface of unused PRS, whereas Fig. F3 shows no Fe on the wear surface of the PRS used with the sample S3. The covering of the wear surface (PRS) by the deposition of other elements is further evidence of the tribological enhancement by the sample S3.

3.7. Results of 3D noncontact optical profilometry for surface roughness

Changes to the surface textures of test specimens after friction tests were quantified in terms of surface roughness, which is correlated with the friction behavior of the utilized sample lubricant. Fig. 11a shows the 2D optical profile for the unused CLS surface, having surface roughness parameters as S_a = 1018 nm and S_q = 2270 nm. The 2D topography is confirmed by the SEM micrograph in Fig. 12a and b as having a surface texture with cross-hatched honing contours.

Optical morphology for the sample S3 is presented in Fig. 11c (S_a = 1084 nm, S_q = 1683 nm). Fig. 11b illustrates 2D roughness profile for the sample S1 (S_a = 1309 nm, S_q = 2252 nm). Thus, sample S3 exhibits a 25 % roughness reduction compared to S1. The presence of nano-additives may have affected the smoothening of the surface texture, attributable to ball bearing effect or protective layer assisting with mending and polishing. Alternatively, there may be a synergistic effect between sliding asperities due to the laminar/spherical morphologies of the nanoparticle additives. Colloidal stability plays a major role in keeping nanoparticles dispersed in the solution. Otherwise, agglomeration leading to large cluster formation will tend to deteriorate the surface texture affecting adversely the tribological behavior of the lubricant.

Reduction of surface roughness or smoothening of surface texture will not guarantee the reduction of wear because the surface smoothening could be either by mending and polishing effect with elastic deformation or by polishing with the removal of nascent layer leading to material removal from the tribo-site. Also, wear would increase the gap between sliding asperities, which could affect the pressure distribution in the fluid. An increasing asperity gap will certainly reduce the COF. On the other hand, an excessive gap between the piston ring cylinder liner interface will lead to compression leak and entry of excessive lubricant into the combustion chamber thereby reducing the mechanical/thermal efficiency of an ICE.

The abrasion loss data were analyzed only for the PRS and CLS test specimens used with reference oil 15W40 (S1) and compared with the unused test specimens. ESI Figs. F4 and F5 present the results of this analysis. Further, SEM, EDX and 3D noncontact profilometry were used to analyze the wear scars of all test specimens.

Using the Bruker ContourX-500 Optical Profilometer, high-resolution measurements of the worn surfaces of PRS and CLS test specimens from sample S1 were obtained. ESI Figs. F4 and F5 illustrate the generated 3D optical profiles with material displacement measurements for the worn surfaces of CLS and PRS, respectively. For S1 the volume is ~ 0.15 mm^3 for CLS (Fig. F4) and ~ − 0.01 mm^3 for PRS (Fig. F5). The wear scar on S1 suggests that this sample sustained the most damage with a minor reduction of surface roughness (~ 0.01 %) during the tribology testing (Figs. 11b, 12c, and d). Therefore, the removed volume of approximately 0.15 mm^3 from the CLS surface could be considered an upper limit for the volume removed from sample S3, which had a smoother surface texture than S1.

3.8. SEM characterization

SEM analysis was used to characterize the morphologies of wear surfaces, which were obtained after LRT tests with selected lubricant samples. All the micrographs are presented with two magnifications with a low magnification image on the left and higher magnification on the right. Fig. 12a & b present the micrographs of unused CLS with 356 × (low) and 2.5 K× (high) magnifications respectively. The images

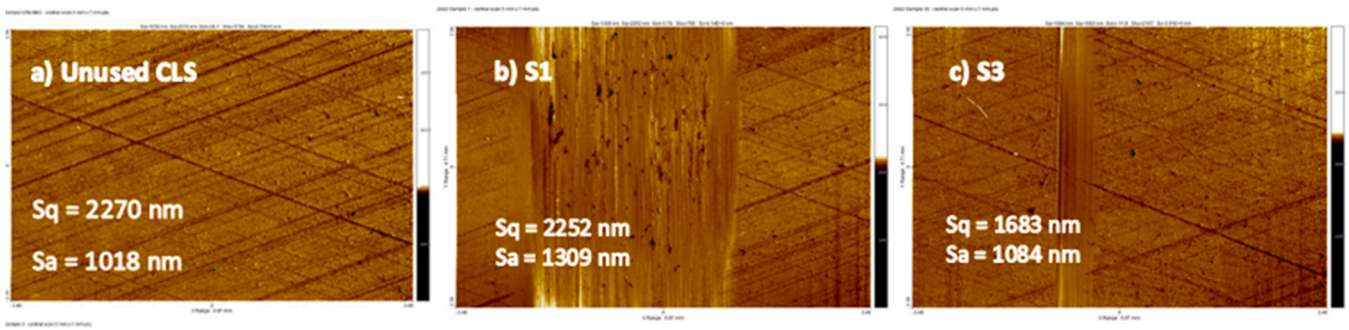

Fig. 11. 2D optical profiles of CLS surfaces before and after the LRT tests; a) unused CLS, b) used with S1, c) used with S3.

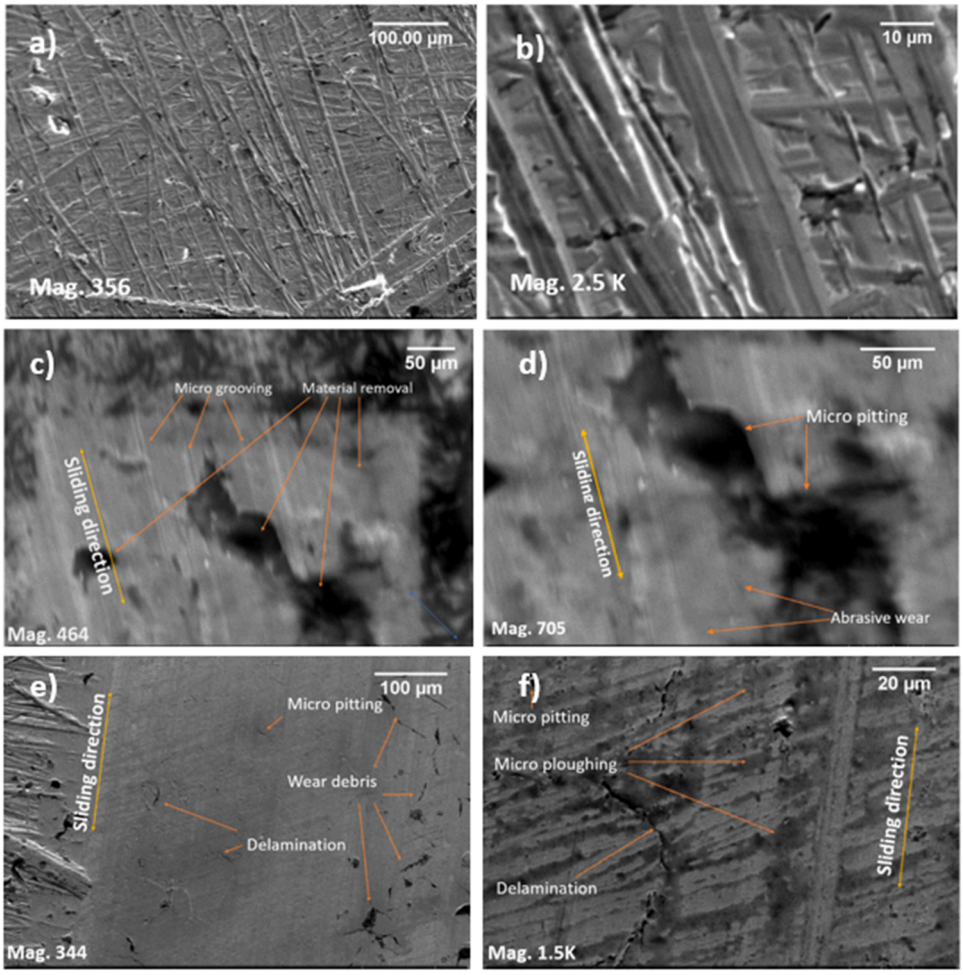

Fig. 12. SEM micrographs for wear surfaces of CLSs before and after LRT tests; a) & b) unused CLS, c) & d) S1-reference oil, e) & f) S3 for low and high magnitudes respectively.

precisely illustrate the cross-hatched honing contours of unused liner surface. The surface texture to entrap lubricant with the sliding of the piston rings to avoid oil-starving condition at TDC. Specifically at boundary and mixed lubrication regimes as a remedy to minimize collision of rubbing asperities in case of failure to produce a protective lubricating film at TDC under decelerating sliding velocity of the piston ring. Micrographs of S1 (Fig. 12c and d) indicate shallow grooving, pitting and abrasive wear leading to material removal from tribo-interface. SEM micrographs of CLS used with S3 are presented with Fig. 12e and f, which demonstrate an enhanced tribological performance by mending and protective layer formation on the friction surface, thus confirming the EDX findings (ESI Fig. F3).

3.9. Specific fuel consumption

Fuel consumption (FC) of S3 was tested along with S1 as reference oil. Tests were done with five break power (load) variations: 5, 10, 14, 17, and 20 kg at 1500 rpm with coolant temperature at ~ 80–100 °C. All the tests were performed in triplicate to minimize errors and the results are presented in Fig. 13. With these results, it is evident that sample S3 is capable of reducing specific fuel consumption (SFC) by 8 % compared to S1. The results, which could be assigned to the ability of S3 to reduce friction compared to S1 (as explained in friction test results, Fig. 9), thus confirming the correlation between friction and fuel consumption of an ICE. The test rig is rated as 4.8 kW (ESI Table T2) but nevertheless tests were extended to 25 % overload condition (~ 6 kW) to study the lubricants characteristics under adverse conditions. Fig. 13 indicates that

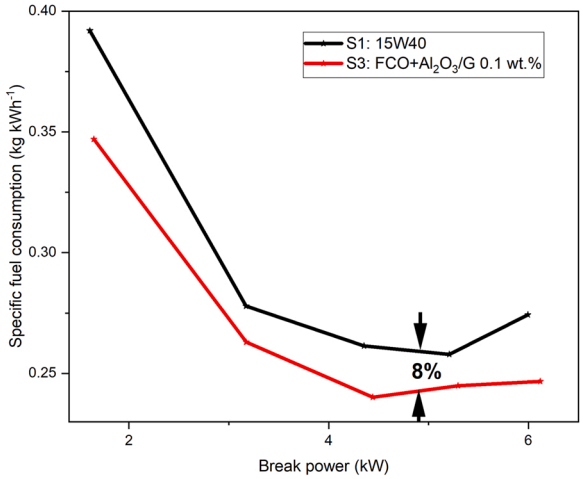

Fig. 13. Break power vs specific fuel consumption analysis for selected samples S1 and S3.

S1 is failing under overload conditions with increasing SFC, where S3 is showing stable SFC confirming the shear stability of FCO based S3, which shed light on the reported rheometric observations above (Fig. 5d).

3.10. Analysis of exhaust emissions

Tests were performed at a constant engine speed of 1500 rpm at ≥ 65.0 % of rated engine load. Test results are presented in Fig. 14, which indicates better pollutant reduction by S3 than S1. Significant reduction of NO and NO_2 concentrations (ppm) by S3 could be attributed to an improved heat transferring ability of S3 compared to S1, which could have had the effect of lowering the combustion temperature causing reduced production of NO_x gases. In addition, S3 generated a reduced production of SO_2 compared to S1. This suggests that the FCO-based S3 does not have any sulfur-containing constituents or thiol groups like S1 (15W40) which could react with O_2 (intake air) to produce sulfuric gases. This observation could also be assigned to creation of sulfate salts by reaction between metal oxides (nanocomposites) of sample formulations and S contents of diesel fuel during combustion. In fact, the SO_2 concentration could arise from the constituents of diesel fuel used to run the test rig.

Sample S3 shows its ability to reduce exhaust pollutants other than CO_2. It is postulated that the ability of a lubricant to transfer heat is not only reduces friction but also reduces production of NO_x emissions. In an ideal ICE operation, there should be reactions between only the constituents of the fuel with intake air inside the combustion chamber, thus emissions should be equal for any lubricant. It is the prime purpose of piston rings to seal the combustion chamber to prevent leakage of compressed air for enhanced thermal and mechanical efficiency. Piston rings also restrict entry of excessive lubricant via this route to the combustion chamber to deter production of hazardous emissions, [15] which is entirely dependent on the mechanical condition, thus maintenance of an engine. However, different quantities of emissions for different lubricants signifies the entry of excessive lubricant quantities to the combustion chamber with the usage of different lubricants. SEM and 3D optical profiles reveal that the morphology of the cylinder liner surface exhibits cross-hatched honed contours to entrap lubricant for lubrication at TDC. Therefore, it is presumed that the formation of a protective layer or a tribo-boundary film by the lubricant will prevent excessive lubricant entry to the combustion chamber, reducing the emission of exhaust pollutants compared to the reference oil S1. For example, formulation S3′s capability to seal the combustion chamber by creating a protective layer on the PRS surface.

4. Conclusion

In this study, we investigated the tribological behavior of lubricants at the piston ring cylinder liner interface of an internal combustion engine considering three different lubrication regimes: elastohydrodynamic, mixed and boundary. To reduce friction and wear under these regimes, a lubricant requires various attributes including density, viscosity, temperature, and pressure dependence of viscosity, thermal, oxidative and shear stability, pour point, cloud point, flash point, fire point, thermal properties, conductivity, neutralization number, surface tension, etc.

The tribological advantages of coconut oil and Al_2O_3/Graphene nano-lubricant (sample S3) are clearly demonstrated through the results of linear reciprocating tribometer (LRT) tests, energy dispersive X-ray spectroscopy (EDX) surface analysis, 3D optical profiles, scanning electron microscopy (SEM) micrographs, specific fuel consumption (SFC) and exhaust gas analyses. Experimental observations reveal a 28 % reduction in overall coefficient of friction (COF), an 8 % reduction of SFC and reductions in CO, SO_2 and NO_x emissions. The dispersion stability and tribological enhancement are attributed to the ultrafine alumina particle size (10.0 ± 0.3 nm), low crystallinity, and a spherical/laminar morphology when hybridized with 2D graphene. EDX analysis revealed deposition of C, Ni, Cr, O, Mo, and K with Al traces on wear surfaces completely covering Fe in the underlying material indicate the formation of protective tribo-film on sliding interface. The phenomenon is further illustrated by SEM images showing the formation of a protective layer on wear surfaces supported by secondary mending and polishing effects. Furthermore, above 50 % of COF reduction at higher sliding velocities, specifically during elastohydrodynamic lubrication (EHL) could be assigned to a rolling or ball bearing effect in-place of

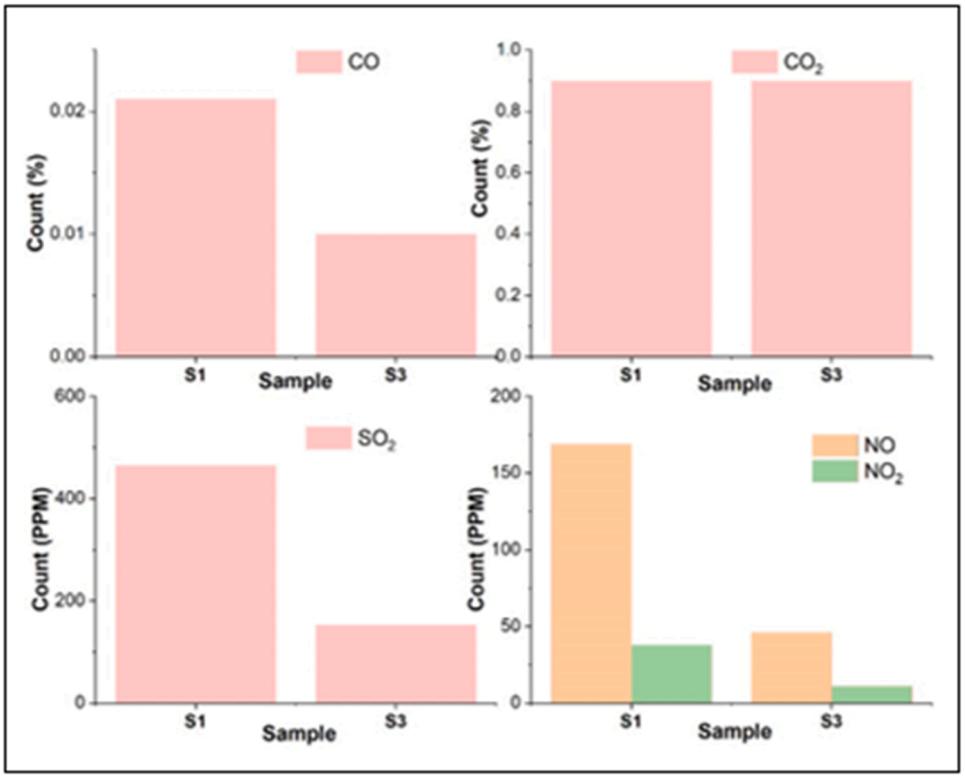

Fig. 14. Results of exhaust gas analysis for sample blends S1 and S3.

sliding lubrication at the sliding interface assigned to the laminar/spherical morphology of Al_2O_3/G nano-additives. Reduced NO_x emissions achieved using S3 lubricant emphasize the comparatively low combustion temperature compared to reference oil (15W40), confirming the improved heat transfer attributes of the optimal Al_2O_3/Graphene nano/bio-lubricant.

Declaration of Competing Interest

The authors declare that they have no known competing financial interests or personal relationships that could have appeared to influence the work reported in this paper.

Data Availability

Data will be made available on request.

Acknowledgement

The authors acknowledge the technical support and experimental facilities at the London South Bank University and Open University, UK. The authors also acknowledge the support offered by Vishal Panchal and Stephen Lewandowski at Bruker Nano Surfaces and Metrology Division, UK.

Appendix A. Supporting information

Supplementary data associated with this article can be found in the online version at doi:10.1016/j.triboint.2023.108619.

References

[1] Gulzar M, Masjuki HH, Kalam MA, Varman M, Zulkifli NWM, Mufti RA, et al. Dispersion stability and tribological characteristics of TiO_2/SiO_2 nanocomposite enriched biobased lubricant. Tribology Trans 2017;60(4):670–80.
[2] Abdulrahiman, KTA, Sajeeb, AM. Characteristical study of coconut oil-based nano-lubricant. In: Proceedings of the international conference on systems, energy & environment (ICSEE) 2019, GCE Kannur, Kerala, July 2019; 2019. Available at SSRN: https://ssrn.com/abstract=3438121 or https://doi.org/10.2139/ssrn.3438121.
[3] Abere JO, Improved performance of bio-lubricants by nanoparticles additives. White rose e-theses, Sheffield, University of Sheffield; 2017.
[4] Talib N, Nasir RM, Rahim EA. Tribological behaviour of modified jatropha oil by mixing hexagonal boron nitride nanoparticles as a bio-based lubricant for machining purposes. J Clean Prod 2017;147:360–78.
[5] Jibin TP, Koshy CP, Mathew MD, Kuriachen B. Tribological characteristic evaluation of coconut oil dispersed with surfactant modified ceria-zirconia hybrid nanoparticles. Tribology - Mater Surf Interfaces 2019;13(4):197–214.
[6] Luo T, Wei X, Huang L, Yang F. Tribological properties of Al_2O_3 nanoparticles as lubricating oil additives. Ceram Int 2014;40(5):7143–9.
[7] Ali MKA, Xianjun H, Mai L, Quingping C, Turkson FR, Bicheng C. Improving the tribological characteristics of piston ring assembly in automotive engines using Al_2O_3 and TiO_2 nanomaterials as nano-lubricant additives. Tribology Int 2016;103:540–54.
[8] Meng Y, Su F, Chen Y. Supercritical fluid synthesis and tribological applications of silver nanoparticle-decorated graphene in engine oil nanofluid. Sci Rep 2016;6:31246.
[9] Song W, Yan J, Ji H. Fabrication of GNS/MoS_2 composite with different morphology and its tribological performance as a lubricant additive. Appl Surf Sci 2019;469(1):226–35.
[10] Song HJ, Jia XH, Li N, Yang XF, Tang H. Synthesis of α-Fe_2O_3 nanorod/graphene oxide composites and their tribological properties. J Mater Chem 2012;22:895–902.
[11] Syahir AZ, et al. A review on bio-based lubricants and their application. J Clean Prod 2017;168:997–1016.
[12] Tung SC, McMillan ML. Automotive tribology overview of current advances and challenges for the future. Tribology Int 2004;37:517–36.
[13] Jia B, Mikalsen R, Smallbone A, Roskilly AP. A study and comparison of frictional losses in free-piston and crankshaft engines. Appl Therm Eng 2018;140(2018):217–24.
[14] Agnieszka J, Joanna J, Joanna K, Antoni K, Wanda Z, Andrzej O. Controlled synthesis of graphene oxide/ alumina nanocomposites using a new dry sol-gel method of synthesis. Chem Pap 2016;71(3):579–95.
[15] Boateng L, Ansong R, Owusu WB, Steiner-Asiedu M. Coconut oil and palm oil's role in nutrition, health and national development: a review. Ghana Med J 2016;50(3):189–96.
[16] Harris RA, Shumbula PM, Walt H v d. Analysis of the interaction of surfactants oleic acid and oleylamine with iron oxide nanoparticles through molecular mechanics modelling. Langmuir 2015;31(13):3934–43.
[17] Mate CM. Chapter 9: lubrication, tribology on the small scale. Oxford UK: Oxford University Press; 2008. p. 207–45.
[18] Stachowiak, GW, Batchelor, AW, Chapter 7: Elastohydrodynamic lubrication. Engineering Tribology, 3rd Ed.; 2005, pp 287–362.
[19] Meng Y, Su F, Chen Y. Supercritical fluid synthesis and tribological applications of silver nanoparticle-decorated graphene in engine oil nanofluid. Sci Rep 2016;6:31246.
[20] Seehra SS, Geddam UK, Schwegler-Berry D, Stefaniak AB. Detection and quantification of 2H and 3R phases in commercial graphene-based materials. Carbon 2015;2015(95):818–23.
[21] Hayes WI, Joseph P, Mughal MZ, Papakonstantinou P. Production of reduced graphene oxide via hydrothermal reduction in an aqueous sulphuric acid suspension and its electrochemical behaviour. J Solid State Electrochem 2014;19:361–80.
[22] Fatijo GG, Smith EH, Sherrington I. Piston-ring film thickness: theory and experiment compared. Proc. IMechE Part J: J Eng Tribol 2016;232(5):550–67.
[23] Pakharukova VP, Yatsenko DA, Gerasimov EYu, Shalygin AS, Martyanov ON, Tsybulya SV. Coherent 3D nanostructure of ɣ-Al_2O_3 simulation of whole X-ray powder diffraction pattern. J Solid State Chem 2017;246:284–92.
[24] Baragau IA, Power NP, Morgan DJ, Heil T, Lobo RA, Roberts CA, et al. Continuous hydrothermal flow synthesis of blue-luminescent, excitation-independent N-doped CQDs as nano-sensors. J Mater Chem A 2020;8(6):3270–9.
[25] Molard LM, Pimenta MA, Dresselhaus G, Dresselhaus MS. Raman spectroscopy in graphene. Phys Rep 2009;473(5–6):51–87.
[26] Jbara AS, Othaman Z, Saeed MA. Structural, morphological and optical investigations of θ-Al_2O_3 ultrafine powder. J Alloy Compd 2017;718:1–6.
[27] Tuschel D. Stress, strain and Raman spectroscopy. J Spectrosc 2019;34(9):10–21.
[28] Baragau IA, Lu Z, Power NP, Morgan DJ, Bowen J, Diaz P, et al. Continuous hydrothermal flow synthesis of S-functionalized carbon quantum dots for enhanced oil recovery. Chem Eng J 2021;405:126631.
[29] Teodorescu CM, Esteva JM, Karnatak RC, Afif El A. An approximation of the Voigt I profile for the fitting of experimental X-ray absorption data. Nucl Instrum Methods Phys Res Sect A: Accel, Spectrom Detect Assoc Equip 1994;345(1):141–7.
[30] Wagner CD, Davis LE, Zeller MV, Taylor JA, Raymond HA, Gale LH. Empirical atomic sensitivity factors for quantitative analysis by electron spectroscopy for chemical analysis. J Surf Interface Anal 1981;3(5):211–25.
[31] Kellici S, Acord J, Ball J, Reehal HS, Morgan D, Saha B. A single rapid route to synthesis of reduced graphene oxide with antibacterial activities. RSC Adv 2014;4:14858–61.
[32] Djebaili K, Mekhalif Z, Boumaza A, Djelloul A. XPS, FTIR, EDX and XRD analysis of Al_2O_3 scales grown on PM2000 alloy. J Spectrosc 2015;2015:1–16.
[33] Mosarof MH, Kalam MA, Masjuki HH, Arslan A, Monirul IM, Ruhul AM, et al. Analysis of thermal stability and lubrication characteristics of Millettia pinnata oil. RSC Adv 2016;6:81414–25.
[34] Azeez S, Bertola V. Lubrication of journal bearings by shear thinning lubricants using different constitutive models. Proc. IMechE Part J: J Eng Tribol 2021;235(6):1203–10.
[35] Stachowiak, GW, Batchelor, AW. Chapter 3 – Lubricants and their composition. Engineering tribology, 3rd Ed.; 2005, pp 51–99.
[36] Liu H, Hou X, Li X, Jiang H, Tian Z, Ali MKA. An experimental study and mechanism analysis on improving dispersion stability performance of Al_2O_3 nanoparticles in base synthetic oil under various mixing conditions. J Nanopart Res 2020;2021(4).